Dielectric, magnetic, and phonon properties of nickel hydroxide

P. Hermet,[1,*] L. Gourrier,[1] J.-L. Bantignies,[1] D. Ravot,[2] T. Michel,[1] S. Deabate,[3] P. Boulet,[4] and F. Henn[1,†]

[1]*Laboratoire Charles Coulomb (UMR CNRS 5221), Université Montpellier II, FR-34095 Montpellier Cédex 5, France*

[2]*Institut Charles Gerhardt (UMR CNRS 5617), Université Montpellier II, FR-34095 Montpellier Cédex 5, France*

[3]*Institut Européen des Membranes (UMR CNRS 5635), Université Montpellier II, FR-34095 Montpellier Cédex 5, France*

[4]*Equipe Chimie Théorique (UMR CNRS 6264), Université de Provence, FR-13397 Marseille, France*

(Received 6 October 2011; revised manuscript received 9 December 2011; published 27 December 2011)

We carried out a complete study (magnetic, electronic, dielectric, dynamic, and elastic properties) of the nickel hydroxide [$Ni(OH)_2$] from first-principles calculations based on density functional theory. No theoretical investigations of these physical properties have been previously reported in literature. Our work supports that $Ni(OH)_2$ is an A-type antiferromagnetic material. In addition, it is negative uniaxial and semiconducting with a direct band gap at the Γ point around 3 eV. By contrast to its electronic dielectric tensor, its static tensor is strongly anisotropic in the plane orthogonal to its optical axis. This anisotropy is mainly governed by a highly polar phonon centered around 510 cm^{-1} and assigned as a rotational E_u mode. Both Raman and infrared spectra have been computed to clarify the longstanding debate on the assignment of the $Ni(OH)_2$ phonon modes reported in literature. All these theoretical results are fruitfully compared to the experimental ones obtained on large $Ni(OH)_2$ "pseudosingle" crystals when available.

DOI: 10.1103/PhysRevB.84.235211 PACS number(s): 31.15.A−

I. INTRODUCTION

Materials for energy storage play a crucial role in sustainable development. Among them, active materials for rechargeable batteries are of peculiar importance since they can store and deliver, in a reversible manner, electrical energy usable in a broad range of daily life equipments, e.g., cell phones, portable computers, electrical vehicles. Efforts in fundamental research and industrial development are therefore concomitantly required for improving their performances with respect to the environmental and economical impacts. Although lithium-ion batteries are nowadays the most efficient systems commercially available for portable equipments, they keep raising problems in regard to (i) applications requiring high capacity and safety as for private and public transportations, (ii) environmental concerns, and (iii) the availability of lithium element on earth. The development of efficient and reliable electrodes made of active material other than lithium is therefore a challenge for the future. In this context, the β-form of nickel hydroxide [$Ni(OH)_2$], which is the active mass of many rechargeable alkaline batteries (e.g., Ni-Cd, Ni-MH, Ni-Zn, Ni-Fe, and Ni-H_2), remains a very resourceful material.

It is well admitted that $Ni(OH)_2$ electrode efficiency relies on its ability to concomitantly exchange a proton and an electron and, hence, is directly dependent on its structural and electrical features.[1–4] However, because of the presence of defects and of heterogeneities throughout the electrode, it is rather difficult to establish a clear connection between the structural state of $Ni(OH)_2$, its conductive properties, and *in fine* its capacity of storing and delivering energy.[5–7] That is one of the main reasons why little is known about the fundamental aspect of the electrochemical process taking place during its oxidation to Ni(OOH) and during the reverse reaction, i.e., reduction. More particularly, one does not know the exact conditions corresponding to the detrimental semiconductor-insulating transition that occurs upon reduction of Ni(OOH) toward $Ni(OH)_2$. To overcome this problem, the $Ni(OH)_2$ phase used in commercial batteries is doped by Co atoms.[8] However, this dopant limits the theoretical capacity, increases the material cost, and is detrimental regarding environmental issues. Furthermore, due to the high density and potential variety of defects, x-ray diffraction analysis remains controversial.[9–16] So, many attempts have been made to get insights in the structure from vibrational spectroscopy (infrared,[17–19] Raman,[7,17,20–24,26–32] and inelastic neutron scattering[17,33]), while mode assignments have never been conclusive. The understanding of these properties and their influences on the electrochemical performances therefore requires considerable experimental or theoretical efforts.[25,34] The latter is not straightforward since, in nickel materials, and more generally in metal transition-based solids, the coupling between electronic and magnetic features must be properly achieved.

In this paper, we perform a complete study of the structural, electronic, magnetic, dynamical, and elastic properties of $Ni(OH)_2$ from first-principles methods based on density functional theory (DFT). Our study therefore covers all the linear couplings between applied static homogeneous electric field, strain, and periodic atomic displacements. Our theoretical results are compared to the experimental ones when available. The main objective of this work is the complete investigation of the microscopic physical properties of $Ni(OH)_2$ for its potential industrial applications. This work can also provide benchmark theoretical results for the understanding of Ni(OOH) and on the NiO_2H_{2-x} intermediate oxidized phases. In particular, this work can be seen as a first step toward the determination of the x stoichiometric parameter corresponding to the insulating-semiconducting transition.

This paper is organized as follows. The next section describes the experimental procedure to investigate the magnetic properties, the lattice dynamic, the electronic band gap, and the static dielectric constant of $Ni(OH)_2$. The theoretical framework of our calculations is given in Sec. III. Section IV is the heart of the paper. In this section, we study first the

magnetic and the electronic band structures of $Ni(OH)_2$ and we compute its Born effective charges and electronic dielectric tensors. Then, we focus on the $Ni(OH)_2$ zone-center phonon modes and we investigate their contributions to its static dielectric tensor and its infrared (IR) reflectivity spectrum. For this purpose, IR and Raman spectra of $Ni(OH)_2$, including both the frequency position and the intensity of phonon peaks, have been computed. The computation of the phonon IR frequencies has been performed not only for the transverse optical (TO) modes, but also for the longitudinal optical (LO) ones. These calculated spectra are sufficiently accurate to be compared to the corresponding experimental ones, and are therefore relevant to clarify the longstanding debate on the assignment of its experimental phonon modes reported in literature. Finally, we report the elastic constants of $Ni(OH)_2$ and estimate its bulk and shear moduli. Section V concludes the paper with the most important results of this work.

II. EXPERIMENTAL CONDITIONS

The $Ni(OH)_2$ compound studied in this work is obtained following the original synthesis route first reported by Scholder and Giesler and then reused by Wallner and Gatterer.[35] The so-obtained material is made of micrometric hexagonal plates constituted by extremely well-ordered hexagonal nanocrystallites. This material shows high crystallinity and a single-crystal-type behavior in μ-Raman spectroscopy due to the coherent orientation of the nanocrystallites' subunits. More details about its synthesis and its structural properties can be found in Gourrier *et al.*[36]

The magnetic characteristics of $Ni(OH)_2$ are studied between 2 K and room temperature, under applied magnetic fields up to 5 T using a SQUID magnetometer from Quantum Design. The mass of the sample was 15.2 mg. To avoid any nonlinear effects, the magnetic susceptibility was obtained under 100 Oe. Zero-field-cooled measurements were performed, between 2 and 300 K, after cooling in zero magnetic field and field-cooled measurements starting from 300 K. In both cases, the temperature step was equal to 2 K. Magnetization was measured at 17, 24, 28, 34, and 300 K. It is a linear function of the magnetic field. No indication of a ferromagnetic ordering is evidenced.

Far- and mid-IR measurements, respectively, in the 50–400 cm^{-1} and 400–4000 cm^{-1} ranges, were carried out in transmission on a Bruker IFS 66V Fourier transform spectrometer. The spectral resolution was 4 cm^{-1} and 64 scans were accumulated. A Si-bolometer cooled at 4 K and a N_2-cooled DTGS detector were, respectively, used to probe the far- and mid-IR domains with extra sensitivity. Measurements were carried out at room temperature on pellets made of a grounded mixture of dried polyethylene (resp. KBr) and 10% (resp. 1%) weight of $Ni(OH)_2$ in the far-IR (resp. mid-IR) range. Diffusive reflectance UV spectra were recorded at room temperature with 2-nm spectral resolution on a Jasco V570 spectrophotometer between 200 and 800 nm.

The static dielectric constant is measured on a disk-shaped pellet (around 1 mm thickness and 13 mm diameter) made of the $Ni(OH)_2$ powder pressed under about 5 tons. Gold electrodes are deposited by sputtering on both parallel faces. The pellet is then placed inside the dielectric spectrometer (Novocontrol BDS-4000) cell between the two parallel metallic electrodes. Measurements are carried out between 1 Hz and 1 MHz at various but fixed temperatures from room temperature to 150 K.

III. COMPUTATIONAL DETAILS

First-principles calculations were performed within the DFT framework as implemented in the ABINIT package.[37] The exchange-correlation energy functional was evaluated within the local spin density approximation (LSDA) using Perdew-Wang parametrization[38] and spin generalized gradient approximation (SGGA) as proposed by Perdew, Burke and Ernzerhof (PBE).[39] All calculations were performed with collinear spins and without LS coupling. The all-electron potentials were replaced by norm-conserving pseudopotentials generated according to the Troullier-Martins scheme,[40] thanks to a package developed at the Fritz-Haber Institute (Berlin).[41] Nickel ($3d^8$ and $4s^2$), hydrogen ($1s^1$), and oxygen ($2s^2$ and $2p^4$) electrons were considered as valence states. Atomic positions have been relaxed until the maximum residual forces on the atoms were less than 5×10^{-6} Ha $Bohr^{-1}$. The electronic wave functions were expanded in plane waves up to a kinetic energy cutoff of 65 Ha. Integrals over the Brillouin zone were approximated by sums over a $8 \times 8 \times 3$ mesh of special k points according to the Monkhorst-Pack scheme.[42] Dynamical matrix, dielectric constants, and Born effective charge (Z^*) tensors were computed within a variational approach to density functional perturbation theory.[43] The Raman susceptibility tensors were obtained within a nonlinear response formalism taking advantage of the $2n+1$ theorem.[44] The infrared and Raman spectra were respectively calculated as described in Refs. 45 and 46.

IV. RESULTS AND DISCUSSION

A. Crystallographic and magnetic structures

Nickel hydroxide crystallizes in the trigonal $P\bar{3}m1$ (D^3_{3d}) space group with the lattice constants $a = 3.13$ Å and $c = 4.63$ Å. Nickel atoms occupy $1a$ Wyckoff position, whereas the oxygen and hydrogen atoms occupy $2d$ Wyckoff positions defined by O($\frac{1}{3}$,$\frac{2}{3}$,z) and H($\frac{1}{3}$,$\frac{2}{3}$,u), where $u = 0.47$ and $z = 0.24$.[47] This structure can be described as a hexagonal close-packed structure of hydroxyl ions (AB oxygen packing) with nickel atoms occupying the octahedral interstices one plane out of two, and the O–H bonds parallel to the c axis (see Fig. 1). The antiferromagnetic (AFM) structure of $Ni(OH)_2$ below 28 K was experimentally evidenced by Szytula *et al.*[47] in 1971 using neutron diffraction, and its magnetic coupling constants have been measured by Enoki *et al.*[48] in 1978. No further experimental nor theoretical studies of the magnetic properties of this material were reported since 30 years. Thus, we take advantage of our recent elaboration of a $Ni(OH)_2$ pseudocrystal constituted of low defects to revisit these magnetic studies.

Figure 2 shows the experimental magnetic susceptibility $\chi = M/H$ of $Ni(OH)_2$ as a function of the temperature. The maximum corresponds to a Néel temperature of $T_N = 26$ K, which is in excellent agreement with the value measured by Szytula *et al.*[47] The linear dependence of the inverse

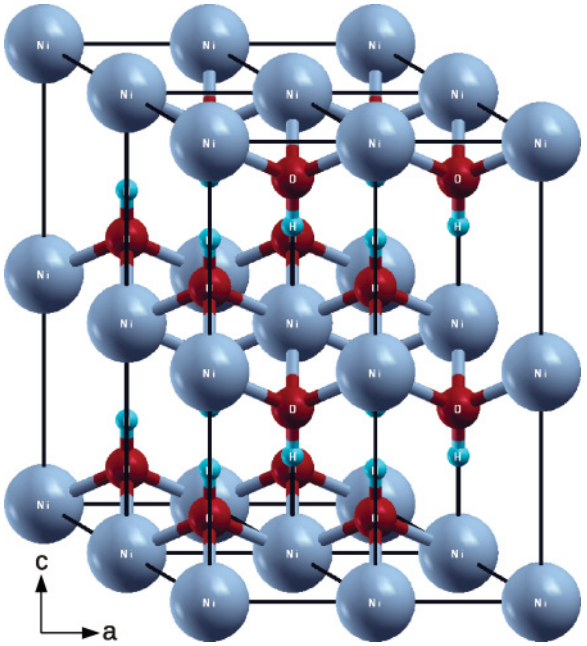

FIG. 1. (Color online) Ideal crystal structure ($2 \times 2 \times 2$ supercell) of $Ni(OH)_2$. This structure is A-type antiferromagnetic with magnetic moments on Ni atoms directed along the c axis.

susceptibility as a function of the temperature is consistent with a Curie-Weiss behavior for a temperature above 150 K (inset of Fig. 2). A linear fit gives a Curie temperature $\theta_p = -22.3$ K and a Curie constant $C = 1.15$ emu K mol^{-1}. These values correspond to an effective paramagnetic moment $\mu_{\text{eff}} = 3.04$ μ_B/Ni ion, which is consistent with the expected value for a high spin d^8 Ni^{2+} ion. The negative value of θ_p indicates that $Ni(OH)_2$ is AFM according to the previous experimental studies.

Selected structural parameters computed using LSDA and SGGA from experimental and relaxed lattice parameters are listed in Table I with the corresponding experimental ones. When the lattice parameters are relaxed, we observe that

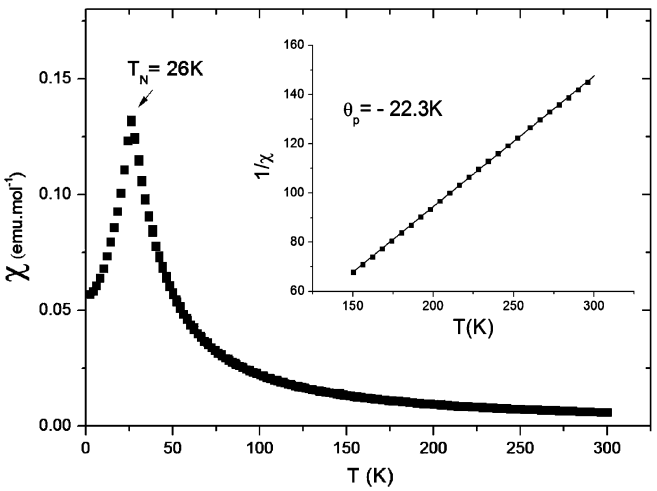

FIG. 2. $Ni(OH)_2$ magnetic susceptibility as a function of the temperature. Inset: Inverse magnetic susceptibility as a function of the temperature.

LSDA predicts a small underestimate of the intralayer lattice parameter (1%), whereas the interlayer one is strongly underestimated (8%). By contrast, SGGA relaxed lattice parameters are closer to the experimental ones since SGGA overcorrect the LSDA predictions, leading to 2%–3% overestimated intralayer and interlayer lattice parameters. Nevertheless, both LSDA and SGGA underestimate the c/a ratio. This unphysical compression of the structure is related to the lack of van der Waals interactions in the exchange-correlation energy functionals.[49] All the bond lengths remain very close by changing the lattice parameters from the experimental values to the theoretical equilibrium ones. The magnetic moment on Ni atoms is quite stable between LSDA and SGGA and whatever the unit-cell volume considered. It is estimated around 1.7–1.8 μ_B (see Table I). Thus, since the best agreement between the calculated structure and the experimental one is obtained at the SGGA level, the different results discussed in the following will be computed using this functional class.

Three magnetic states of $Ni(OH)_2$ have been considered to investigate its most probable magnetic ground state: a ferromagnetic (FM) and two AFM states, respectively called A and C type. The C-type AFM state (CAFM) corresponds to FM ac layers antiferromagnetically coupled along the b direction, whereas the A-type AFM state (AAFM) corresponds to FM ab layers with AFM coupling along the c direction. This AAFM state is the magnetic ground state of $Ni(OH)_2$ experimentally observed by Szytula *et al.*[47] In all cases, we use the experimental lattice parameters to obtain the energy of these three magnetic states, and their values Δ are reported relative to the AAFM state. We found that the AAFM magnetic ordering is predicted as the most stable spin configuration (in agreement with the observed magnetic ground state), followed by the FM ($\Delta = 1.363$ meV) and the CAFM ($\Delta = 3.061$ meV) magnetic orderings.

The intralayer magnetic interactions between nickel ions are of the exchange type and they take place through the oxygens.[47] Thus, the intralayer magnetic coupling constant J_1 can be calculated according to an Ising model where we developed the magnetic Hamiltonian

$$H = -J_1 \sum_{\langle ij \rangle} S_{zi} S_{zj}, \tag{1}$$

up to the first ($\langle ij \rangle$) nearest Ni neighbors. S_{zi} stands for the z component of the total spin on the magnetic center i. We restricted our study to intralayer magnetic interactions because the nature (superexchange or dipolar types) of the interlayer (second-nearest Ni neighbors J_2) interactions are unclear. Within our sign convention used in the Ising model, a positive value of the magnetic coupling constant indicates a FM exchange, whereas a negative value corresponds to an AFM case. J_1 can be obtained from the energy differences between the CAFM and FM states. Taking into account that there are six first-nearest Ni neighbors per unit cell and using a high spin $S = 1$ on Ni atoms, J_1 becomes $J_1 = (E_{\text{CAFM}} - E_{\text{FM}})/8$, where E_{CAFM} and E_{FM} are, respectively, the energy of the CAFM and FM states. We found $J_1/k_B = 2.46$ K, where k_B is the Boltzmann constant. This predicted value is in good agreement with the experimental one [2.70 K (Ref. 48)]. In addition, the positive sign of J_1 is correctly calculated,

TABLE I. Selected structural parameters, magnetic moment, and electronic band gap of AAFM $Ni(OH)_2$ calculated from DFT at experimental and relaxed lattice parameters and using LSDA and SGGA. Corresponding experimental data are also reported. μ is an estimate of the local magnetic moment on Ni atoms.

	SGGA		LSDA		
	Fixed expt.	Relaxed	Fixed expt.	Relaxed (Ref. 47)	Expt.
a (Å)	3.13	3.22	3.13	3.10	3.13
c (Å)	4.63	4.71	4.63	4.26	4.63
c/a	1.479	1.465	1.479	1.374	1.479
Ni-O (Å)	2.090	2.120	2.062	2.047	2.121
O-H (Å)	0.964	0.964	0.974	0.976	1.065
Ni-O-Ni (deg)	96.98	98.70	98.74	98.57	95.07
μ (μ_B)	1.77	1.78	1.67	1.67	2.0 ± 0.2
E_g (eV)	2.90	2.70	2.05	2.15	~3.0–3.5[a]

[a]From our UV measurements.

indicating FM intralayer interactions as expected by the AAFM ground state of $Ni(OH)_2$.

B. Electronic band structure

Figure 3 displays the computed electronic band structure of $Ni(OH)_2$ along the Γ-A-H-K-Γ-M-L-H line, together with its total DOS between −20 and 35 eV. This calculation has been performed at experimental lattice parameters. The top of the valence band was fixed to 0 eV. The top of the valence band and the bottom of the conduction band are both located at the Γ point. A plane-wave pseudopotential DFT approach therefore predicts $Ni(OH)_2$ as a semiconducting material with a direct band gap estimated at $E_g = 2.90$ eV. In addition, when calculations are performed at the SGGA relaxed volume, the band-gap position is not affected and its value is not significantly sensitive (2.70 eV). This band-gap prediction is consistent with our experimental value of $E_g \sim 3.0$–3.5 eV measured from UV spectroscopy.

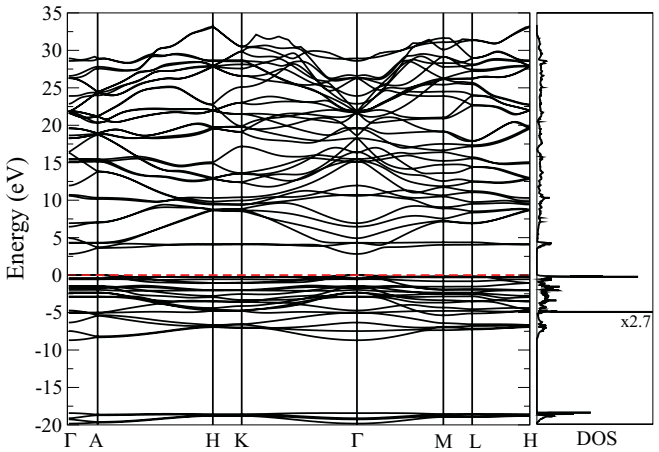

FIG. 3. (Color online) Electronic band structure and total DOS of $Ni(OH)_2$ computed at the SGGA level and at experimental volume between −20 and 35 eV. The horizontal dashed line indicates the position of the Fermi level.

C. Dielectric properties

In the following, the orthogonal reference system (x,y,z) is chosen such as z is aligned along the $Ni(OH)_2$ trigonal axis and x is aligned along the crystallographic a axis. Due to the hexagonal symmetry, the different tensors are diagonal with two independent components labeled $xx = yy = \perp$ and $zz = \parallel$.

1. Electronic dielectric tensor

The electronic dielectric permittivity tensor ε^∞ is related to a second derivative of the electronic energy with respect to an electric field, and it has been computed using a linear response technique. No scissor correction has been included in the calculation. Its computed values are $\varepsilon^\infty_\perp = 3.55$ and $\varepsilon^\infty_\parallel = 3.30$, corresponding to a refractive index of [1.88, 1.88, 1.82]. $Ni(OH)_2$ is therefore a negative uniaxial trigonal crystal with a quite isotropic electronic response to a homogeneous electric field. Unfortunately, there are no available experimental or theoretical data reported in literature on its dielectric properties for comparison purposes. However, although DFT strongly overestimates the values of ε^∞ with respect to the experimental ones,[50] we expect that our calculated values of ε^∞ should be close to the experimental ones. This is a consequence of the observed good agreement between the calculated and measured band-gap energies.

2. Born effective charges

Z^* components are reported in Table II. The acoustic sum rule $\sum_\kappa Z^*_{\alpha\beta}(\kappa) = 0$ is fulfilled in our calculations within a slight deviation from charge neutrality, which is less than 0.001 $|e|$, suggesting well-converged calculations. Z^* are a

TABLE II. Independent elements of Born effective charge tensors (Z^*) on the different atoms constitutive of $Ni(OH)_2$ computed using SGGA at experimental volume (in $|e|$).

	$Z^*_\perp$	$Z^*_\parallel$
Ni	2.086	1.593
O	−1.405	−1.270
H	0.362	0.473

dynamical quantity strongly influenced by dynamical changes of orbital hybridization induced by atomic displacements. The components of these tensors therefore reflect the effects of covalency or ionicity with respect to some reference ionic value. As a consequence, their amplitude is not directly related to that of the static charges and can take anomalous values. In the following of the discussion, we assume that the reference ionic values of Ni, O, and H atoms in $Ni(OH)_2$ are $+2$, -2, and $+1$, respectively. We observe that all Z^* tensors are anisotropic. This fact reflects the topology of the chemical bonds in the structure and indicates that the charge transfer is significantly different along and perpendicular to the trigonal axis. The $Z^*_\perp$(Ni) value is close to the ionic charge expected on Ni atoms. By contrast, all the other values of Z^* on the atoms are almost 40% smaller than their ionic charges. These results suggest that in the plane perpendicular to the trigonal axis, Ni atoms have an ionic configuration, whereas we have weak covalent Ni–O or O–H bonds along the trigonal axis.

3. Static dielectric tensor

The electronic dielectric permittivity tensor describes the response of the electron gas to a homogeneous electric field if the ions are taken as fixed at their equilibrium positions. To include the response of the crystal lattice to the electric field, one can use a model that assimilates the solid to a system of undamped harmonic oscillator. In this condition, the static dielectric tensor ε^0 is decomposed into an electronic and an ionic term such as

$$\varepsilon^0_{\alpha\alpha} = \varepsilon^\infty_{\alpha\alpha} + \frac{4\pi}{\Omega_0}\sum_m \frac{S_{\alpha\alpha}(m)}{\omega_m^2}. \quad (2)$$

The infrared oscillator strengths $\tilde{S}$ is a second-order tensor given by

$$S_{\alpha\alpha}(m) = \left|\sum_{\gamma,\kappa} Z^*_{\alpha\gamma}(\kappa) u_\gamma(\kappa,m)\right|^2, \quad (3)$$

where the sum runs over all atoms κ and space directions γ, $u_\gamma(\kappa,m)$ and ω_m are, respectively, the $(\gamma\kappa)$ component of the eigendisplacement vector and the frequency of the mth mode obtained from the diagonalization of the analytical part of the dynamical matrix, and Ω_0 is the unit-cell volume. The computed values of the mode oscillator strengths are reported in Table III for a $Ni(OH)_2$ monocrystal.

TABLE III. Phonon contributions of the infrared TO phonon modes of $Ni(OH)_2$ to its static dielectric constant (ε^0). Mode oscillator strengths ($\tilde{S}$) are also reported in the table ($\times 10^{-5}$ a.u.). Frequencies (ω_m) are in cm^{-1}. All these quantities are computed using SGGA at the experimental volume.

	E_u modes			A_{2u} modes		
	ω_m	$S_\perp$	$\varepsilon^0_\perp$	ω_m	$S_\parallel$	$\varepsilon^0_\parallel$
ε^∞			3.55			3.30
TO1	354	7.00	0.64	418	13.39	0.88
TO2	496	56.78	2.64	3643	62.18	0.05
Total (ion)			3.28			0.93
Total			6.83			4.23

The computed values at 0 K of ε^0 are $\varepsilon^0_\perp = 6.83$ and $\varepsilon^0_\parallel = 4.23$. Its average (5.96) is overestimated with respect to the experimental value (4.1) measured at 150 K and 1 MHz on a powder. This overestimate is linked to the ionic term, and it is mainly due to discrepancies between the calculation of the IR oscillator strengths and the corresponding experimental ones (see next section). By contrast to ε^∞, the inclusion of the ionic contribution leads to a strong anisotropy of ε^0 with $\varepsilon^0_\parallel$ much smaller than $\varepsilon^0_\perp$. The component values of these tensors show that the dielectric response of $Ni(OH)_2$ is mainly electronic along the optical axis, whereas it is both electronic and ionic in the plane orthogonal to this axis. From the decomposition of ε^0, we observe that the E_u(TO2) and A_{2u}(TO2) modes, respectively calculated at 496 and 3643 cm^{-1}, represent the most important contribution of the oscillator strength (Table III). However, due to their different frequencies, they do not contribute equally to ε^0. The main contribution (39%) comes from the E_u(TO2) mode, whereas less than 2% is expected from the A_{2u}(TO2) mode. Thus, the strong anisotropy of ε^0 is governed by the E_u(TO2) mode. Furthermore, the two modes cited above dominate the IR absorption spectrum of $Ni(OH)_2$ with intense bands due to their dominant oscillator strengths in agreement with experimental data (see next part).

D. Zone-center optical phonon modes

The zone-center optical phonon modes of $Ni(OH)_2$ can be classified according to the irreducible representations of D_{3d} point group into $2A_{1g} \oplus 2E_g \oplus 2A_{2u} \oplus 2E_u$. The A_{2u} and E_u modes are IR actives and respectively polarized along and perpendicular to the trigonal axis. The A_{1g} and E_g modes are Raman actives. In this work, we used the notation from Mitra[51] to assign all these zone-center optical phonon modes. In this notation, a letter T or R, respectively, labeling translational or rotational lattice modes (see Fig. 4), is added after its irreducible representation.

Within our orthogonal reference system, Raman susceptibility tensors have a well-defined form given by[52]

$$A_{1g} = \begin{pmatrix} a & & \\ & a & \\ & & b \end{pmatrix}, \quad (4)$$

$$E_g = \begin{pmatrix} c & & \\ & -c & d \\ & d & \end{pmatrix}, \quad \begin{pmatrix} & -c & -d \\ -c & & \\ -d & & \end{pmatrix}. \quad (5)$$

Several measurements have been carried out to assign the IR and Raman modes of $Ni(OH)_2$ in the last decade. However, in spite of these numerous experimental investigations, their assignments are not yet unambiguously established in the literature and some controversies remain between the authors. Furthermore, there are no theoretical phonon investigations of $Ni(OH)_2$ material presently available in literature, excepted the paper from Kazimirov *et al.* recently published.[34] However, the work of these authors is restricted to inelastic neutron scattering and they do not fix the debate about the assignment of its lattice modes. Thus, we have performed the calculation of Raman and IR bands (TO and LO frequencies) taking into account of their intensities, and we used both LSDA and SGGA

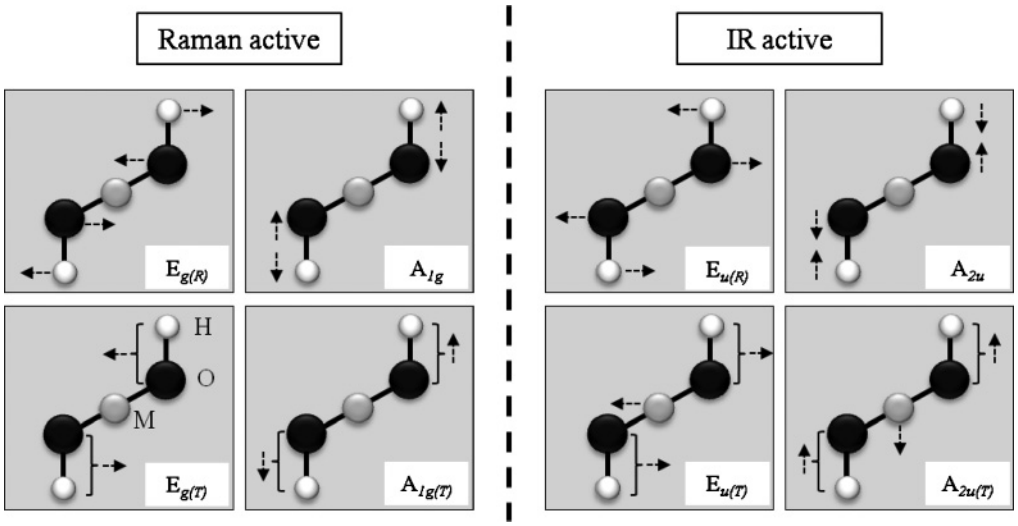

FIG. 4. Representation of normal modes of brucite-type $M(OH)_2$ material according to Mitra notation (Ref. 51). *R* and *T* are rotational and translational lattice modes, respectively.

exchange-correlation (XC) functionals to estimate the dependence of the XC class on the phonon frequency calculation. Lattice parameters have been fixed to the experimental ones to eliminate any volume effects on the phonon calculation between these two functionals. Tables IV and V report our calculated TO phonon frequencies using LSDA and SGGA, together with the available experimental ones. We observe that the SGGA frequencies differ from the LSDA ones within 5% discrepancy. Thus, our calculations should unambiguously clarify the available phonon assignments reported in the literature, and they should accurately predict the phonon frequencies that still remain experimentally undetected.

1. Raman modes

Various assignment schemes have been proposed for the $Ni(OH)_2$ Raman lines. This comes from the fact that Raman spectroscopy is very sensitive to small modifications in the structure and to the stoichiometry of the material. Table IV summarizes our calculated phonon frequencies classified according to their symmetry with the available experimental data reported in literature.

In the region of the NiO lattices modes (Fig. 5, left), two lines are always observed at 310 and 445 cm^{-1},[17,26–32] in agreement with the calculation. According to all authors, we assign these two lines as translational lattice modes. Nevertheless, their accurate symmetries are not unambiguously established in the literature. Indeed, most authors respectively assign the lines centered at 310 and 445 cm^{-1} to have $E_{g(T)}$ and $A_{1g(T)}$ symmetry,[26–30] whereas Murli *et al.*[32] suggest the inverse assignment. Our calculation does not support the assignments of Murli *et al.* and supports the assignments of the other authors. The last remaining experimental E_g line is observed either around 510 or 880 cm^{-1} in the literature with different assignments. When it is observed at 510 cm^{-1}, it is assigned to the presence of structural defects[26] and/or to a $E_{g(R)}$ mode.[27,29] By contrast, when it is observed at 880 cm^{-1}, it is assigned as the $E_{g(R)}$ mode.[32,33] Our calculation predicts this last $E_{g(R)}$ line at 840 cm^{-1} and no line is predicted around 510 cm^{-1}, confirming our attribution for the latter as defects.

In the region of the hydroxyl stretching vibrations (Fig. 5, left), two lines are observed (one intense line around 3570 cm^{-1} and one small line around 3600 cm^{-1}), whereas the calculation predicts only one intense line centered at 3550 cm^{-1} (average of LSDA and SGGA frequencies). The most intense line is unambiguously assigned to have A_{1g} symmetry according to all authors. The small experimental

TABLE IV. Calculated (experimental volume) and experimental Raman frequencies (in cm^{-1}) of $Ni(OH)_2$ with their corresponding assignments.

Calculations (present)				Experiments					
LSDA		SGGA		Refs. 26–30		Ref. 32		Ref. 17	
310	$E_{g(T)}$	316	$E_{g(T)}$	310	$E_{g(T)}$	315	$A_{1g(T)}$	313	$E_{g(R)}$
425	$A_{1g(T)}$	445	$A_{1g(T)}$	445	$A_{1g(T)}$	450	$E_{g(T)}$	447	$A_{1g(T)}$ or $E_{g(T)}$
				510	$E_{g(R)}$	517		508	$A_{1g(T)}$ or $E_{g(T)}$
843	$E_{g(R)}$	868	$E_{g(R)}$			880	$E_{g(R)}$		
3503	A_{1g}	3600	A_{1g}	3570	A_{1g}	3580	A_{1g}	3581	A_{1g}
				3600		3600		3601	
				3680					

TABLE V. Calculated (experimental volume) and experimental infrared TO frequencies (cm^{-1}) of $Ni(OH)_2$ with their corresponding assignments. Calculated LO frequencies are between parentheses.

Calculations (present)				Experiments					
LSDA		SGGA		Ref. 19		Ref. 18		Ref. 17	
356 (370)	$E_{u(T)}$	354 (366)	$E_{u(T)}$	348	$E_{u(T)}$	350	$E_{u(T)}$	332	$E_{u(R)}$
408 (443)	$A_{2u(T)}$	418 (469)	$A_{2u(T)}$	451	$A_{2u(R)}$	452	$A_{2u(T)}$	440	$E_{u(T)}$ or $A_{2u(T)}$
516 (642)	$E_{u(R)}$	496 (665)	$E_{u(R)}$	549	$E_{u(R)}$	530	$E_{u(R)}$	530	$E_{u(T)}$ or $A_{2u(T)}$
3543 (3572)	A_{2u}	3643 (3673)	A_{2u}	3635	A_{2u}	3639	A_{2u}	3636	A_{2u}

line centered at 3600 cm^{-1} has been assigned to the stretching vibrations of hydroxyl groups located near structural defect sites[26,31] or to isolated water molecules adsorbed at the surface of the $Ni(OH)_2$ nanocrystallites.[27] Furthermore, an additional line is sometimes reported around 3680 cm^{-1} in badly crystallized material and ascribed to free OH groups located at the nanocrystallite surface.[26] We support the possible assignment of these two latter lines because they are not expected by our calculation, so that they can not be intrinsic to $Ni(OH)_2$ material.

2. *Infrared modes*

According to the group theory, four IR bands are expected. By contrast to the Raman modes, three IR bands are quite well observed by all the authors around 332, 530, and 3636 cm^{-1} and their symmetry is consistent between them. The last remaining band centered around 440 cm^{-1} is controversial since it can be assigned as translational[18] or rotational[19] lattice mode.

The calculated IR spectrum is displayed in Fig. 6 with the experimental one. We observe a qualitative good agreement between the calculated and experimental spectra. Indeed, the $E_{u(R)}$ (530 cm^{-1}) and A_{2u} (3636 cm^{-1}) bands are correctly predicted both in position and relative intensity, and have the strongest intensities. The $A_{2u(T)}$ experimental band centered around 440 cm^{-1} appears weaker on the calculated spectrum than on the experimental one. However, this effect is not related to its intrinsic mode oscillator strength. It is rather a consequence of the fact that the $E_{u(R)}$ band at 530 cm^{-1} in the experimental spectrum is quite broad and that it overlaps with the A_{2u} band centered at 450 cm^{-1}, whereas this is not the case for the calculated spectrum since we use a constant linewidth to represent the IR bands. Thus, these four IR bands are unambiguously assigned by our calculations, and their assignments are consistent with those reported by all authors in literature. In addition, we have fixed the assignment of the band centered around 430 cm^{-1} as translational A_{2u} lattice mode.

At the Γ point, the macroscopic electric field splits the polar active modes into TO and LO modes. No experimental investigation of this LO-TO splitting is presently reported in the literature. Thus, we have calculated the IR reflectivity spectra to have an estimate of the LO-TO splitting strength in $Ni(OH)_2$. The reflectivity of optical waves normal to the surface, with their electric field along an optical axis of the crystal **q**, is given by[54]

$$R(\omega) = \left(\frac{\epsilon_{\hat{q}}^{1/2}(\omega) - 1}{\epsilon_{\hat{q}}^{1/2}(\omega) + 1} \right)^2, \tag{6}$$

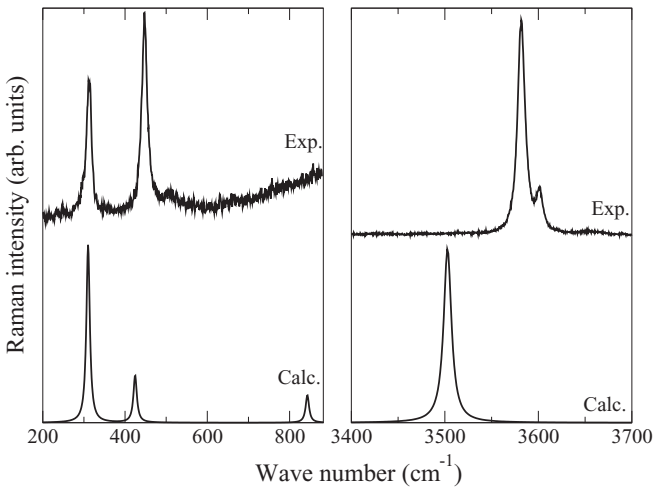

FIG. 5. Calculated and experimental Raman spectra of polycrystalline $Ni(OH)_2$. The experimental spectrum is recorded at room temperature and from Ref. 17. The calculated spectrum is computed at the LSDA level (Ref. 53), using the experimental volume and with a constant linewidth fixed at 3 cm^{-1}.

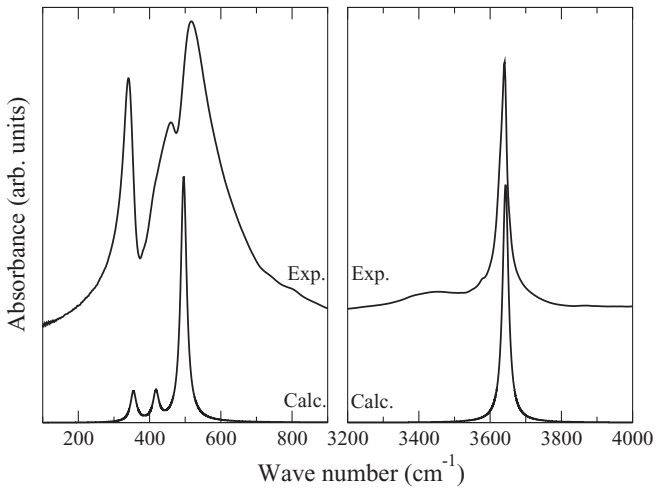

FIG. 6. Calculated and experimental infrared spectra of polycrystalline $Ni(OH)_2$. The experimental spectrum is recorded at room temperature. The calculated spectrum is computed at the SGGA level, using the experimental volume and with a constant linewidth fixed at 8 cm^{-1}.

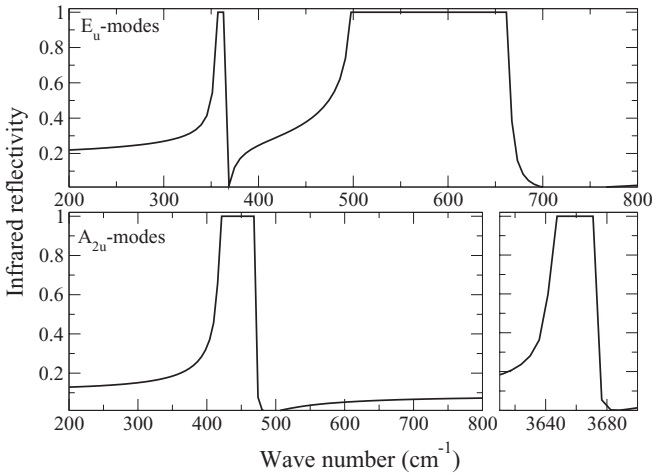

FIG. 7. SGGA infrared reflectivity spectra of $Ni(OH)_2$ monocrystals computed at the experimental volume.

where the dielectric tensor is obtained as

$$\epsilon_{\hat{q}}(\omega) = \sum_{\alpha} \hat{q}_\alpha \epsilon^{\infty}_{\alpha\alpha}(\omega)\hat{q}_\alpha + \frac{4\pi}{\Omega_0} \sum_{m} \frac{\sum_\alpha \hat{q}_\alpha S_{\alpha\alpha}(m)\hat{q}_\alpha}{\omega_m^2 - \omega^2}. \quad (7)$$

Figure 7 displays the calculated IR reflectivity spectra of A_{2u} and E_u modes. The reflectivity related to the A_{2u} modes is observed when the electric field is parallel to the trigonal axis of the crystal [i.e., perpendicular to the (100) or (010) surfaces]. Similarly, the E_u modes can be observed when the electric field is perpendicular to the trigonal axis [i.e., perpendicular to the (001) surface]. Since our approach neglects the damping of the phonon modes, their reflectivities saturate to 1. As expected from the frequency calculation of the TO and LO modes, we observe that the LO-TO splitting is significant (more than 20 cm^{-1}) for all modes in $Ni(OH)_2$, and its value can even reach more than 100 cm^{-1} for the E_u modes around 500 cm^{-1}. The frequencies of the LO modes obtained by the calculation are also reported in Table V. The eigenvectors of the polar TO modes do not necessarily correspond to those of their corresponding LO modes due to the long-range Coulomb interactions. We therefore calculated the overlap matrix between the eigenvectors of the TO and LO IR modes using the following equation:

$$\left\langle \mathbf{u}_m^{\mathrm{LO}} \middle| M \middle| \mathbf{u}_n^{\mathrm{TO}} \right\rangle = \sum_{\gamma,\kappa} u_m^{\mathrm{LO}}(\kappa\gamma) M_\kappa u_n^{\mathrm{TO}}(\kappa\gamma), \quad (8)$$

where M_κ is the mass of the κth atom, and $\mathbf{u}_m^{\mathrm{LO}}$ and $\mathbf{u}_n^{\mathrm{TO}}$ are the eigendisplacement vectors of the mth LO and nth TO modes, respectively. The overlap matrix (not reported) between the eigenvectors of the E(TO) [resp. A_{2u}(TO)] and E(LO) [resp. A_{2u}(LO)] modes show that their mixing is, however, negligible. Thus, each LO mode can therefore be associated to its corresponding TO mode as reported in Table V.

E. Elastic properties and mechanical stability

Elastic constants characterize the ability of a material to deform under small stresses. They can be described by a fourth-rank tensor (C) relating the second-rank stress tensor (σ) to the (also second-rank) strain tensor (η) via the generalized Hooke law

$$C_{\alpha\beta} = \frac{\partial \sigma_\alpha}{\partial \eta_\beta}, \quad (9)$$

where $\alpha,\beta = 1,2,\ldots,6$ denote the Cartesian directions given in Voigt notation. The above equation can be split into two main contributions:

$$C_{\alpha\beta} = \left.\frac{\partial \sigma_\alpha}{\partial \eta_\beta}\right|_u + \sum_{\kappa} \frac{\partial \sigma_\alpha}{\partial u_\alpha(\kappa)} \frac{\partial u_\alpha(\kappa)}{\partial \eta_\beta}. \quad (10)$$

The first term is the frozen (clamped) ion elastic tensor ($\bar{C}$), whereas the second term includes contributions from force-response internal stress and displacement-response internal strain tensors. The second term also accounts for the ionic relaxations in response to strain perturbations. The addition of the two contributions is the relaxed ion elastic tensor C.

Due to the D_{3d} point group of $Ni(OH)_2$, these tensors have only 6 independent elements to be determined instead of 21. The independent elements of the clamped-ion and relaxed-ion elastic tensors at constant electric field are reported in Table VI, together with their corresponding compliance tensors ($\bar{S}$ and S), with the compliance tensors being defined as the inverse of the elastic tensors. These results show that the physical elastic constants (C) are generally smaller than the frozen-ion ones (at least for diagonal elements) since the additional internal relaxation allows some of the stress to be relieved. Similarly, the diagonal S values are larger than the $\bar{S}$ ones, reflecting the increased compliance allowed by the relaxation of the atomic coordinates. In addition, $Ni(OH)_2$ is mechanically stable because the elastic tensor constants satisfy Born mechanical stability restrictions for trigonal structure given by the following system of inequations:[55]

$$\begin{aligned} C_{11} - |C_{12}| &> 0, \\ (C_{11} + C_{12})\, C_{33} - 2C_{13}^2 &> 0, \\ (C_{11} - C_{12})\, C_{44} - 2C_{14}^2 &> 0. \end{aligned} \quad (11)$$

Bulk (B) and shear (G) moduli can estimate the hardness of a material in an indirect way:[56] materials with high B or G are likely to be hard materials. On the basis of Voigt approximation, we have calculated these quantities using the

TABLE VI. Calculated clamped-ion ($\bar{C}$) and relaxed-ion (C) elastic tensors (in GPa), and corresponding compliance tensors ($\bar{S}$ and S, in 10^{-2} GPa^{-1}) of $Ni(OH)_2$. The indexes denote the Cartesian directions given in Voigt notation. All these quantities are computed at the theoretical volume and using SGGA functional.

Index	$\bar{C}$	C	$\bar{S}$	S
11	185.70	151.20	0.66	0.79
12	74.70	58.55	−0.26	−0.29
13	50.91	12.16	−0.05	−0.18
14	−7.47	−2.23	0.13	0.11
33	439.66	33.15	0.24	3.15
44	52.97	22.44	1.92	4.48

following relations:[57]

$$B = \tfrac{1}{9}[2(C_{11} + C_{12}) + C_{33} + 4C_{13}], \quad (12)$$

$$G = \tfrac{1}{30}(7C_{11} - 5C_{12} + 2C_{33} - 4C_{13} + 12C_{44}). \quad (13)$$

The corresponding predicted values are B =55.70 GPa and G =35.09 GPa. The typical relations between B and G are $G \simeq 1.1B$ and $0.6B$ for covalent and ionic materials, respectively. In our case, the calculated value of G/B is 0.63, indicating that $Ni(OH)_2$ is an ionic material in agreement with Z^* analysis.

V. CONCLUSION

In this paper, we have investigated the electronic, magnetic, dielectric, dynamical, and elastic properties of $Ni(OH)_2$ within the DFT framework. Our study covers all the linear couplings between applied static homogeneous electric field, strain, and periodic atomic displacements: Born effective charge, dynamical matrix at the zone-center, dielectric, and elastic tensors. The investigation of the magnetic ground state of $Ni(OH)_2$ shows that this material has an A-type AFM order as experimentally observed. The band structure of $Ni(OH)_2$ states that this material is a semiconductor with a direct band gap at Γ point around 3 eV. Its electronic dielectric tensor is nearly isotropic, whereas its static dielectric tensor is strongly anisotropic in the plane orthogonal to the optical axis of this material. This anisotropy is governed by a specific phonon assigned as a rotational E_u mode centered around 510 cm^{-1}. An exhaustive attribution of the optical IR and Raman modes is given for the first time. The calculation of the complete set of zero-pressure elastic constants has been performed and satisfies the Born mechanical stability criteria for trigonal materials. We have also reported and discussed the IR reflectivity spectra and the zone-center phonon frequencies of TO and LO modes. One of the important outcomes of this study is that our DFT-based calculations are well supported, qualitatively and quantitatively, by the experimental data we obtained on a well-crystallized β-hydroxide material in respect to its magnetic, electric/dielectric, and vibrational features. This extremely favorable comparison undoubtedly validates the calculation and the approach led in this work. We do now possess the theoretical tool to get deeper insights into the $Ni(OH)_2$ electrochemical behavior and more particulary into the insulator-semiconductor transition, which occurs at an intermediate and unknown oxidation state between $Ni(OH)_2$ and Ni(OOH).

ACKNOWLEDGMENTS

The authors are grateful to SAFT research for its financial support and to A. Mauger for helpful discussions. L.G., J-L.B., S.D. and F.H. would also like to thank the french national research agency (ANR) for its financial support via the Stock-E funding programme.

*Correspondences and requests should be sent to P. H. for the DFT calculations.

†Correspondences and requests should be sent to F. H. for the experimental measurements.

[1] D. M. Mac Arthur, J. Electrochem. Soc. **117**, 422 (1970).
[2] J. W. Weidner and P. Timmerman, J. Electrochem. Soc. **141**, 346 (1994).
[3] B. Paxton and J. Newman, J. Electrochem. Soc. **143**, 1287 (1996).
[4] S. Motupally, C. C. Streinz, and J. W. Weidner, J. Electrochem. Soc. **145**, 29 (1998).
[5] C. Leger, C. Tessier, M. Menetrier, C. Denage, and C. Delmas, J. Electrochem. Soc. **146**, 924 (1999).
[6] S. Deabate and F. Henn, Electrochim. Acta **50**, 2823 (2005).
[7] S. Deabate, F. Fourgeot, and F. Henn, Electrochim. Acta **51**, 5430 (2006).
[8] V. Pralong, Y. Habre, A. Delahaye-Vidal, and J. M. Tarascon, Solid State Ionics **147**, 73 (2002).
[9] A. Delahaye-Vidal, B. Beaudoin, N. Sac-Epée, K. Tekaia-Elhsissen, A. Audemer, and M. Figlarz, Solid State Ionics **84**, 239 (1996).
[10] C. Delmas and C. Tessier, J. Mater. Chem. **7**, 1439 (1997).
[11] C. Tessier, P. H. Haumesser, P. Bernard, and C. Delmas, J. Electrochem. Soc. **146**, 2059 (1999).
[12] M. Rajamathi, P. V. Kamath, and R. Seshadri, J. Mater. Chem. **10**, 503 (2000).
[13] T. N. Ramesh, R. S. Jayashree, and P. V. Kamath, Clays and Clay Minerals **51**, 570 (2003).
[14] G. S. Thomas and P. V. Kamath, J. Chem. Sci. **118**, 127 (2006).
[15] T. N. Ramesh, P. V. Kamath, and C. Shivakumara, Acta Crystallogr., Sect. B: Struct. Sci. **62**, 530 (2006).
[16] T. N. Ramesh and P. V. Kamath, Mater. Res. Bull. **43**, 3227 (2008).
[17] J.-L. Bantignies, S. Deabate, A. Righi, S. Rols, P. Hermet, J.-L. Sauvajol, and F. Henn, J. Phys. Chem. C **112**, 2193 (2008).
[18] C. Mockenhaupt, T. Zeiske, and H. D. Lutz, J. Mol. Struct. **443**, 191 (1998).
[19] E. F. De Oliveira and Y. Hase, Vib. Spectrosc. **31**, 19 (2003).
[20] B. Cornilsen, P. J. Karjala, and P. L. Loyselle, J. Power Sources **22**, 351 (1988).
[21] M. C. Bernard, M. Keddam, H. Takenouti, P. Bernard, and S. Senyarich, J. Electrochem. Soc. **143**, 2447 (1996).
[22] M. C. Bernard, P. Bernard, M. Keddam, S. Senyarich, and H. Takenouti, Electrochim. Acta **41**, 91 (1996).
[23] R. Kostecki and F. McLarnon, J. Electrochem. Soc. **144**, 485 (1997).
[24] S. Deabate, F. Fourgeot, and F. Henn, J. Power Sources **87**, 125 (2000).
[25] A. Van der Ven, D. Morgan, Y. S. Meng, and G. Ceder, J. Electrochem. Soc. **153**, A210 (2006).
[26] M. C. Bernard, R. Cortes, M. Keddam, H. Takenouti, P. Bernard, and S. Senyarich, J. Power Sources **63**, 247 (1996).
[27] A. Audemer, A. Delahaye, R. Farhi, N. Sac-Epee, and J. M. Tarascon, J. Electrochem. Soc. **144**, 2614 (1997).

[28]F. P. Kober, J. Electrochem Soc. **114**, 215 (1967).
[29]J. F. Jackovits, in *Proceedings of the Symposium on the Nickel Electrode*, edited by R. G. Gunther and S. Gross (The Electrochemical Society, Pennington, NJ, 1982), Vol. 82–4, pp. 48–68.
[30]C. Johnston and P. R. Graves, Appl. Spectrosc. **44**, 105 (1990).
[31]B. Cornilsen, X. Shan, and P. L. Loyselle, J. Power Sources **29**, 453 (1990).
[32]C. Murli, S. M. Sharna, S. K. Kulshreshtha, and S. K. Sikka, Phys. B (Amsterdam) **307**, 111 (2001).
[33]R. Baddour-Hadjean, F. Fillaux, and J. Tomkinson, Phys. B (Amsterdam) **213**, 637 (1995).
[34]V. Y. Kazimirov, M. B. Smirnov, L. Bourgeois, L. Guerlou-Demourgues, L. Servant, A. M. Balagurov, I. Natkaniec, N. R. Khasanova, and E. V. Antipov, Solid State Ionics **181**, 1764 (2010).
[35]H. Wallner and K. Gatterer, Z. Anorg. Allg. Chem. **628**, 2818 (2002).
[36]L. Gourrier, S. Deabate, T. Michel, M. Paillet, P. Hermet, J.-L. Bantignies, and F. Henn, J. Phys. Chem. C **115**, 15067 (2011).
[37]X. Gonze, B. Amadon, P. M. Anglade, J. M. Beuken, F. Bottin, P. Boulanger, F. Bruneval, D. Caliste, R. Caracas, M. Cote, T. Deutsch, L. Genovese, Ph. Ghosez, M. Giantomassi, S. Goedecker, D. Hamann, P. Hermet, F. Jollet, G. Jomard, S. Leroux, M. Mancini, S. Mazevet, M. J. T. Oliveira, G. Onida, Y. Pouillon, T. Rangel, G. M. Rignanese, D. Sangalli, R. Shaltaf, M. Verstraete, G. Zerah, and J. W. Zwanziger, Comput. Phys. Commun. **180**, 2582 (2009).
[38]J. P. Perdew and Y. Wang, Phys. Rev. B **45**, 13244 (1992).
[39]J. P. Perdew, K. Burke, and M. Ernzerhof, Phys. Rev. Lett. **77**, 3865 (1996).
[40]N. Troullier and J. L. Martins, Phys. Rev. B **43**, 1993 (1991).
[41]M. Fuchs and M. Scheffler, Comput. Phys. Commun. **119**, 67 (1999).
[42]H. J. Monkhorst and J. D. Pack, Phys. Rev. B **13**, 5188 (1976).
[43]X. Gonze and C. Lee, Phys. Rev. B **55**, 10355 (1997).
[44]M. Veithen, X. Gonze, and Ph. Ghosez, Phys. Rev. Lett. **93**, 187401 (2004).
[45]P. Hermet, J. L. Bantignies, J. L. Sauvajol, and M. R. Johnson, Synth. Met. **156**, 519 (2006).
[46]P. Hermet, N. Izard, A. Rahmani, and Ph. Ghosez, J. Phys. Chem. B **110**, 24869 (2006).
[47]A. Szytula, A. Murasik, and M. Balanda, Phys. Status Solidi B **43**, 125 (1971).
[48]T. Enoki and I. Tsujikawa, J. Phys. Soc. Jpn. **45**, 1515 (1978).
[49]V. Barone, M. Biczysko, and M. Pavone, Chem. Phys. **346**, 247 (2008).
[50]X. Gonze, Ph. Ghosez, and R. W. Godby, Phys. Rev. Lett. **74**, 4035 (1995).
[51]S. S. Mitra, in *Solid State Physics*, edited by F. Seizt and D. Turnbull (Academic, New York, 1962), Vol. 13.
[52]R. Loudon, Adv. Phys. **13**, 423 (1964).
[53]Only LSDA is presently available inside the ABINIT code to compute the intensity of the Raman lines.
[54]L. D. Landau and E. M. Lifschitz, *Electrodynamics of Continuous Media* (Pergamon, New York, 1960).
[55]J. S. Tse and D. D. Klug, Phys. Rev. Lett. **67**, 3559 (1991).
[56]L. D. Landau and E. M. Lifschitz, *Theory of Elasticity*, 3rd ed. (Pergamon, Oxford, 1986).
[57]W. Voigt, *Lehrbuch der Kristallphysik* (Teubner, Leipzig, 1928).